J. Fluid Mech. (1986), *vol.* 166, *pp.* 305–324
Printed in Great Britain

Route to chaos in porous-medium thermal convection

By S. KIMURA, G. SCHUBERT
Department of Earth and Space Sciences, University of California, Los Angeles, CA 90024, USA

AND J. M. STRAUS
Space Sciences Laboratory, The Aerospace Corporation, P.O. Box 92957, Los Angeles, CA 90009, USA

(Received 12 February 1985 and in revised form 11 December 1985)

A pseudo-spectral numerical scheme is used to study two-dimensional, single-cell, time-dependent convection in a square cross-section of fluid saturated porous material heated from below. With increasing Rayleigh number R convection evolves from steady S to chaotic NP through the sequence of bifurcations $S \rightarrow P^{(1)} \rightarrow QP_2 \rightarrow P^{(2)} \rightarrow NP$, where $P^{(1)}$ and $P^{(2)}$ are simply periodic regimes and QP_2 is a quasi-periodic state with two basic frequencies. The transitions (from onset of convection to chaos) occur at Rayleigh numbers of $4\pi^2$, 380–400, 500–520, 560–570, and 850–1000. In the first simply periodic regime the fundamental frequency f_1 varies as $R^{\frac{1}{2}}$ and the average Nusselt number $\overline{Nu}$ is proportional to $R^{\frac{1}{3}}$; in $P^{(2)}$, f_1 varies as $R^{\frac{1}{4}}$ and $\overline{Nu} \propto R^{\frac{11}{16}}$. Convection in QP_2 exhibits hysteresis, i.e. if the QP_2 state is reached from $P^{(1)}$ ($P^{(2)}$) by increasing (decreasing) R then the frequency with the largest spectral power is the one consistent with the extrapolation of f_1 according to $R^{\frac{1}{2}}$ ($R^{\frac{1}{4}}$). The chaotic states are characterized by spectral peaks with at least 3 fundamental frequencies superimposed on a broadband background noise. The time dependence of these states arises from the random generation of tongue-like disturbances within the horizontal thermal boundary layers. Transition to the chaotic regime is accompanied by the growth of spectral components that destroy the centre-symmetry of convection in the other states. Over-truncation can lead to spurious transitions and bifurcation sequences; in general it produces overly complex flows.

1. Introduction

It is well known that with increasing Rayleigh number a thermally convecting fluid layer undergoes a sequence of transitions to chaotic flow. The experiments of Gollub & Benson (1980) identify 4 routes to turbulence depending on the geometrical aspect ratio of the layer and the Prandtl number of the fluid. All of these paths begin with a bifurcation from a steady state (S) to an oscillatory periodic flow (P), gradually evolve toward more complex time-dependent flows, and end in a chaotic state characterized by a frequency spectrum with significant broadband noise. The sequence of transitions constitutes a monotonic progression toward increasing disorder.

Although less is known about the transitions that occur with increasing Rayleigh number when time-dependent thermal convection takes place in a layer of fluid-saturated porous material heated from below, enough has been learned to appreciate

that the routes to chaos in porous-medium convection are fundamentally different from those in the convection of ordinary fluids. The most significant difference is that the sequence of events occurring in porous-medium convection is not characterized by monotonically increasing disorder. The two-dimensional states that can exist in a square cross-section of fluid-saturated porous material (the situation to which this paper is addressed) evolve with Rayleigh number through the sequence $S \rightarrow P^{(1)} \rightarrow QP_2 \rightarrow P^{(2)}$ (Schubert & Straus 1982), where QP_2 is a quasi-periodic state with 2 basic frequencies and the superscripts on P simply indicate different regimes. The $QP_2 \rightarrow P^{(2)}$ transition is a reverse transition from a more-disordered to a less-disordered state. Similar behaviour has been noted in Hele–Shaw convection (Koster & Müller 1984), which is perhaps not surprising since inertial forces are negligible in both the porous-medium and Hele–Shaw cases.

According to Schubert & Straus (1982), the second single-frequency regime exists in the Rayleigh-number R range from about $R_4 = 530$ to at least $R = 650$, the highest value of R they considered (R_1, R_2, R_3 and R_4 denote the values of R at the onset of convection, the $S \rightarrow P^{(1)}$ transition, the $P^{(1)} \rightarrow QP_2$ transition, and the reverse $QP_2 \rightarrow P^{(2)}$ bifurcation respectively). The fate of this simply periodic flow as R is increased above 650 has remained unknown, however. Our primary objective in the work reported here has therefore been to extend our knowledge of the nature of time-dependent porous-medium convection to higher Rayleigh numbers. We are particularly concerned with identifying the transitions that follow the $QP_2 \rightarrow P^{(2)}$ reverse bifurcation at $R = R_4$ and determining if chaos lies somewhere at the end of this sequence.

In order to facilitate the computations at high Rayleigh numbers we have developed a numerical code based on the pseudo-spectral method (Orszag 1971; Gottlieb & Orszag 1977) that is more efficient than the Galerkin code used in Schubert & Straus (1982). With this new code we have been able to accurately simulate single-cell porous-medium convection with unity aspect ratio for Rayleigh numbers as high as 1200. We have confirmed previous results, in particular the bifurcations $P^{(1)} \rightarrow QP_2$ and $QP_2 \rightarrow P^{(2)}$ at R_3 and R_4, by employing much higher resolution. We have discovered a fifth transition, at a Rayleigh number $R = R_5$ that lies somewhere between 850 and 1000, which marks the end of the second simply periodic regime and the beginning of a second multiple-frequency regime. This high-R multiple-frequency regime differs fundamentally from the low-Rayleigh-number QP_2 regime in that the former contains a significant broadband spectral component. On this basis we classify the high-R multiple-frequency regime as chaotic.

In the next section we briefly discuss the mathematical formulation of the problem and the pseudo-spectral numerical method used in its solution. Section 3 contains the results of our numerical experiments. It gives the sequence of bifurcations that takes steady convection to chaos with increasing Rayleigh number. It also describes each of the distinct time-dependent convection regimes that are encountered on the route to chaos. Section 4 discusses more general aspects of the numerical results. It focuses on the physical processes involved in the generation of time dependence. In the concluding remarks we emphasize the consequences of over-truncation in producing spurious transitions.

2. Mathematical formulation

The mathematical background is identical to that of Straus (1974), Straus & Schubert (1979, 1981), and Schubert & Straus (1979, 1982) and only a brief

description will be given here. With the assumption that Darcy's law and the Boussinesq approximation are valid, it is possible to derive a single differential equation for the dimensionless stream function ϕ_ξ of the two-dimensional flow

$$\frac{\partial}{\partial\tau}\nabla^2\phi+\phi_{\zeta\xi}\nabla^2\phi_\xi-\phi_{\xi\xi}\nabla^2\phi_\zeta=\nabla^4\phi+R\phi_{\xi\xi}. \tag{2.1}$$

The associated boundary conditions are

$$\phi_{\xi\xi}=\phi_{\zeta\zeta}=0 \quad (\zeta=0,1), \tag{2.2}$$

$$\phi_{\xi\zeta}=\nabla^2\phi_\xi=0 \quad (\xi=0,1). \tag{2.3}$$

In (2.1)–(2.3), τ is a non-dimensional time and ξ and ζ are dimensionless horizontal and vertical coordinates respectively. The lengthscale is the thickness of the porous layer d, and the timescale is $d^2\rho c/k$, where k is the average thermal conductivity of the fluid and the solid matrix, ρ is the fluid density, and c is the specific heat of the fluid. The dimensionless horizontal and vertical velocities are given by $\phi_{\xi\zeta}$ and $-\phi_{\xi\xi}$ respectively. The Rayleigh number R is defined by

$$R=\frac{\alpha g\rho^2 Kcd\Delta T}{\mu k}, \tag{2.4}$$

where K is the permeability of the porous marix, α is the coefficient of thermal expansion of the fluid, g is the gravitational acceleration, μ is the fluid viscosity, and ΔT is the excess temperature of the bottom boundary relative to the top boundary. The imposed boundary conditions correspond to impermeable and isothermal top ($\zeta=1$) and bottom ($\zeta=0$) boundaries and insulated vertical walls ($\xi=0,1$).

The solution for ϕ can be written as an eigenfunction expansion with basis functions obtained from the solution of the linear part of (2.1) subject to the boundary conditions (2.2) and (2.3)

$$\phi(\tau,\zeta,\xi)=\sum_{n=1}^{\infty}\sum_{j=0}^{\infty}\Phi_{nj}(\tau)\sin n\pi\zeta\cos j\pi\xi. \tag{2.5}$$

The substitution of (2.5) into (2.1) yields an infinite set of coupled, nonlinear, first-order ordinary differential equations for the spectral coefficients Φ_{nj}. These equations are truncated with $n+j\leqslant N$, where N is a positive integer already referred to as the truncation number, and solved numerically.

We will characterize the time-dependent solutions by the Nusselt number

$$Nu=\frac{q}{k\Delta T/d}=1-\sum_{n=1}^{\infty}\frac{n^2\pi^2}{R}\Phi_{n0}, \tag{2.6}$$

where q is the horizontally averaged upward heat flux. For a given R we calculate $Nu(\tau)$ and determine its spectral content by means of a fast-Fourier-transform algorithm. The Nusselt-number time series is computed for τ large enough, typically as large as $\tau=1$, that we can accurately identify the frequencies of any peaks contained in the power spectrum. We also ensure that the frequencies and amplitudes of spectral peaks are independent of the overall length of the time integration.

The main difficulty in applying the Galerkin method to (2.1) is the evaluation of convolution products arising from the nonlinear terms; overall computation time is proportional to N^4 in the two-dimensional problem. The pseudo-spectral method used here, also known as the collocation method or the method of selected points, bypasses the evaluation of convolution products and is thereby more efficient in computing

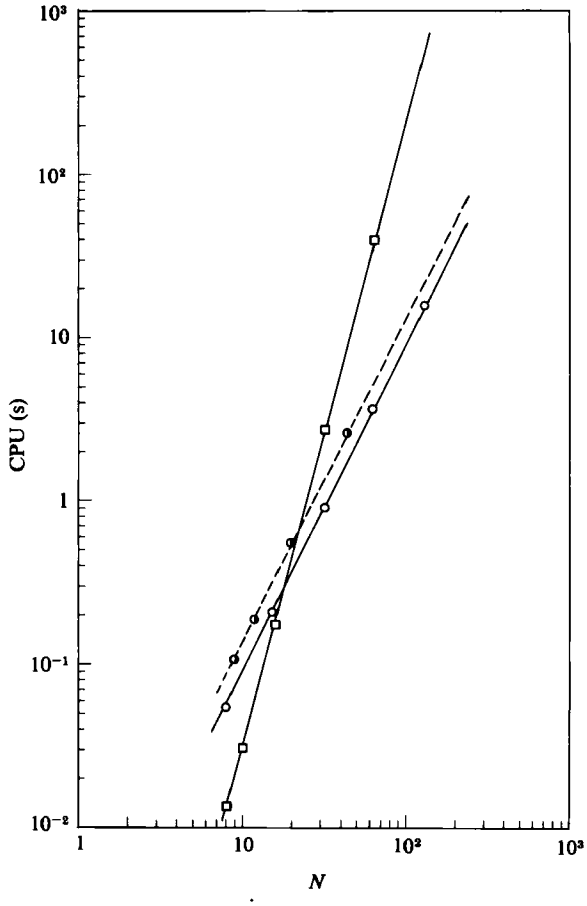

FIGURE 1. Comparison between the Galerkin code and the pseudo-spectral code to assess the relative speeds of the methods: ○, the pseudo-spectral code with truncation numbers $N = 2^m$, where m is an integer; ◑, the pseudo-spectral code with truncation numbers $N \neq 2^m$; □, the Galerkin code. The Euler method was used in both codes. The plotted CPU(s) (IBM 370/3033) is the computation time required to advance a specified $\Delta\tau$. $\Delta\tau$ is identical for both codes.

the nonlinear terms. The pseudo-spectral code has been extensively tested against the Galerkin code of Straus (1974).

The Galerkin code used by Schubert & Straus (1982) explicitly enforces the symmetry condition that the only non-zero Φ_{jn} are those for which $j+n$ is a non-zero even integer. This is not required in the pseudo-spectral code, which allows non-symmetric modes to grow freely. However, we found that the spectral coefficients representing the non-symmetric modes generally did not grow; instead, the values of these coefficients remained negligibly small except for a few cases with very high Rayleigh numbers. This will be discussed in greater detail later in the paper.

Figure 1 shows the computation time required to advance one *a priori* specified time step $\Delta\tau$ in the Galerkin and pseudo-spectral codes as a function of truncation number N (the same $\Delta\tau$ and identical time integration schemes are used in both codes). The speeds of the two codes are comparable at relatively low values of the truncation number. However, the pseudo-spectral code is much faster at the large truncation levels required to simulate convection at very high Rayleigh numbers. For example, the pseudo-spectral code is roughly 40 times faster at $N = 128$ and would be 1300

times faster at $N = 1024$. In the range of truncation numbers typical for the present study ($N = 30$–56), the pseudo-spectral code runs roughly 7 times faster than the Galerkin code. Most of the calculations reported here were carried out on the VAX 11/780 minicomputer using double precision (14 significant figures).

3. Characteristics of time-dependent solutions at high Rayleigh number

Transition 1: *Onset of steady convection* S

The critical Rayleigh number R_1 for the onset of steady single-cell convection S in a square cross-section is $4\pi^2$ (Lapwood 1948).

Transition 2: $\mathrm{S} \rightarrow \mathrm{P}^{(1)}$

Single-cell convection is steady for Rayleigh numbers less than a second critical value R_2, whereas for $R \geqslant R_2$ it is simply periodic $\mathrm{P}^{(1)}$ with a single frequency f_1. It is difficult to determine the precise value of R_2 because of the necessity of prohibitively long time integrations. Schubert & Straus (1982), using the Galerkin technique with $N = 18$, concluded that R_2 lies between 380 and 400. Caltagirone's (1974) numerical results gave $R_2 = 385$. At values of $R > R_2$ the frequency f_1 increases with R according to $f_1 \propto R^{\frac{1}{2}}$ as shown in figure 2.

Figure 3 shows the streamlines and isotherms at successive intervals of time during a single oscillation of the flow at $R = 500$. Tongue-like deformations of the thermal boundary layers are responsible for the oscillatory behaviour. They are most readily visible in the isotherm patterns as bumps in boundary-layer isotherms. The disturbances grow in amplitude as they are advected towards the corners, and they can be seen in the vertical plumes that form when the boundary layers are forced to turn the corners. The core of the flow experiences a significant alteration during the oscillation; this is most evident in the stream-function patterns.

Transition 3: $\mathrm{P}^{(1)} \rightarrow \mathrm{QP}_2$

The third transition takes place by the introduction of a subfrequency f_2 in addition to the primary frequency f_1. The primary frequency f_1 has an $R^{\frac{1}{2}}$ Rayleigh-number dependence similar to the frequency in the simply periodic regime that exists at $R < R_3$ (see figure 2). Indeed, f_1 in the double-frequency regime is a continuous extension of f_1 in the single-frequency regime, while the frequency f_2 is less than a third of f_1. The bifurcation Rayleigh number R_3 depends upon the truncation number. With $N = 18$, R_3 is between 480 and 500 (Schubert & Straus 1982), but both $N = 26$ and $N = 30$ give a single-frequency solution at $R = 500$ and a double-frequency state at $R = 520$. Our best estimate for R_3 is somewhere between 500 and 520.

Figure 4 shows (*a*) $Nu(\tau) - \overline{Nu}$ and its (*b*) power spectrum at $R = 540$. All the spectral peaks occur at frequencies that are sums and differences of the two fundamental frequencies f_1 and f_2 and their harmonics. The powers and frequencies of the spectral peaks are listed in table 1. It is perhaps significant that the spectral peak at $f^* = f_1 + f_2$ lies exactly on the extension of the $R^{\frac{1}{2}}$ trend defined by the frequency of the second simply periodic regime (figure 2) that we discuss below.

Streamline and isotherm patterns for a typical QP_2 state at $R = 540$ are shown in figure 5. Disturbances to the thermal boundary layer are particularly evident in the isotherms while the streamlines clearly illustrate the variability in the core flow. One of the examples shows an instant when there are two rotating cells in the core. The clear variability in the core flow is characteristic of the $\mathrm{P}^{(1)}$ and QP_2 time-dependent regimes.

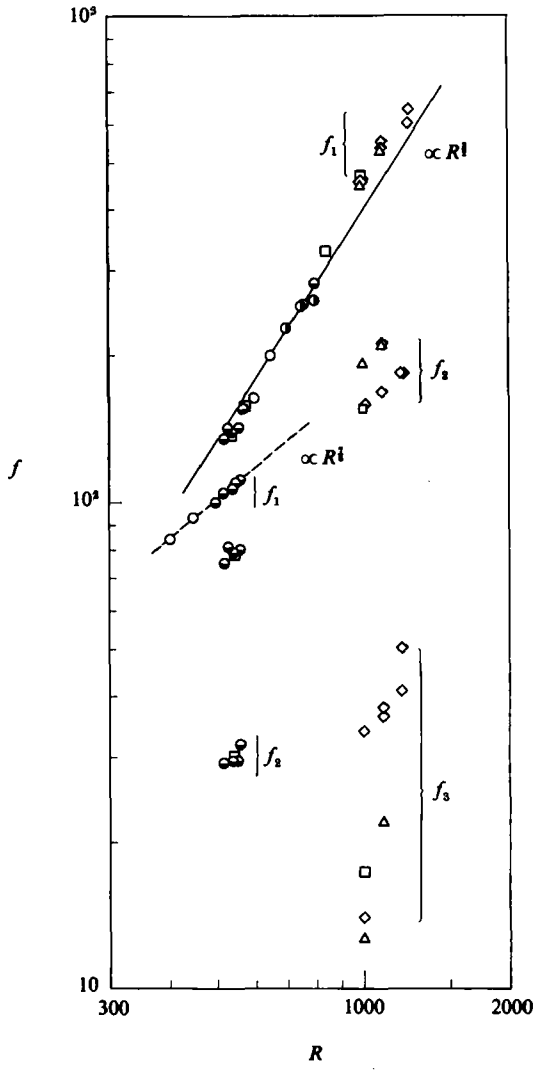

FIGURE 2. Dimensionless frequencies f of the peaks in the power spectra of $Nu(\tau)$. ○, $N = 18$; ◑, 20; ◒, 26; □, 30; △, 36; ◇, 42. The primary frequency f_1 in the first simply periodic regime approximately fits to the power law $R^{\frac{1}{2}}$, while in the second single-frequency regime f_1 follows the trend $R^{\frac{1}{2}}$. The subfrequency f_2 is shown in the first multiple-frequency regime. Subfrequencies f_2 and f_3 are shown for the second multiple-frequency regime. The different values of f_2 and f_3 at $R = 1000$ and 1100 for the truncation levels 30, 36 and 42 are due to different initial conditions. The large scatter in f_3 is probably due to poor frequency resolution at these low frequencies.

We have found that the solutions in QP_2 exhibit hysteresis. With the exception of the solution for $R = 530$, all of our results were obtained by employing a solution at a lower R to provide the initial conditions for a higher-Rayleigh-number case. The solution at $R = 530$ was obtained by using a solution at a higher R in the second P-regime (discussed below) to provide initial conditions. According to table 1, at $R = 530$ the spectral peak with the highest power is at $f = 147$ and the one with the second highest power is at $f = 81$. This is not what would be expected from an interpolation of the results at $R = 520$ and $R = 540$ (table 1). The primary frequency

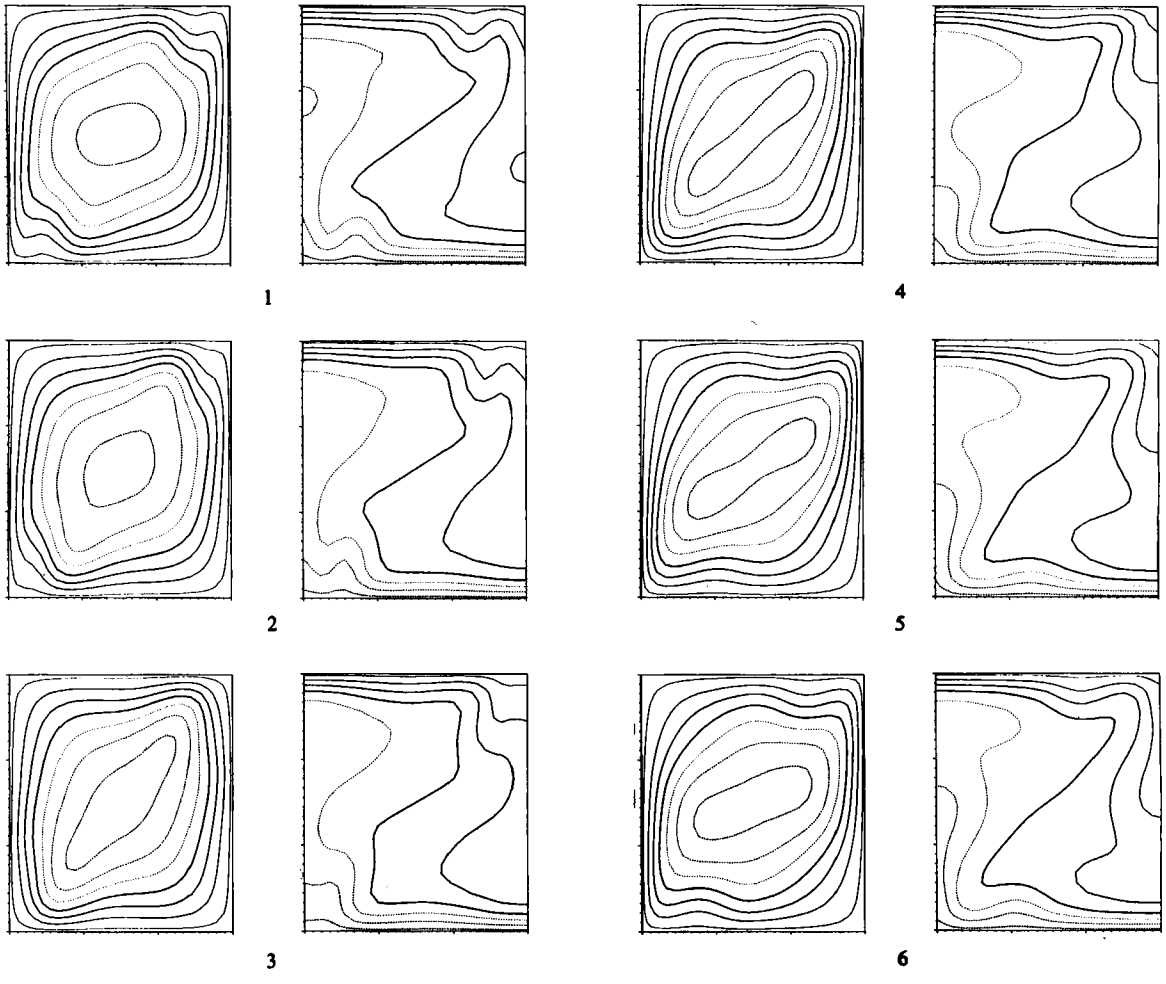

FIGURE 3. Streamline and isotherm patterns at $R = 500$ during a single oscillation ($N = 26$). The non-dimensional time interval between successive figures is 0.0015 and the total elapsed time is 0.009 ($\tau_1 \equiv 1/f_1 = 0.01$). The isotherm contour interval is 0.15. The stream-function ϕ_ξ contour interval is 2.5.

$f = 150$ at $R = 530$ is more consistent with an extension to lower R of the $f \propto R^{\frac{3}{2}}$ trend characteristic of the second simply periodic regime (figure 2). Since the primary frequencies (the ones with the highest spectral powers) at $R = 520$, 540, 550 and 560 are consistent with the $f \propto R^{\frac{1}{2}}$ trend of the first simply periodic regime (figure 2) we conclude that the solutions in QP_2 depend on the paths by which they are arrived at.

The variances in the $Nu(\tau)$ power spectra of the QP_2 solutions are distinguished by relatively large values (figure 6). Schubert & Straus (1982) reported that the variance goes through a strong minimum between $R = 520$ and 600. This study locates the minimum at $R = 570$.

Transition 4: $\mathrm{QP}_2 \rightarrow \mathrm{P}^{(2)}$

A reverse transition from multiple frequency to single frequency occurs at the fourth bifurcation Rayleigh number R_4, which we estimate to be between 560 and 570 for

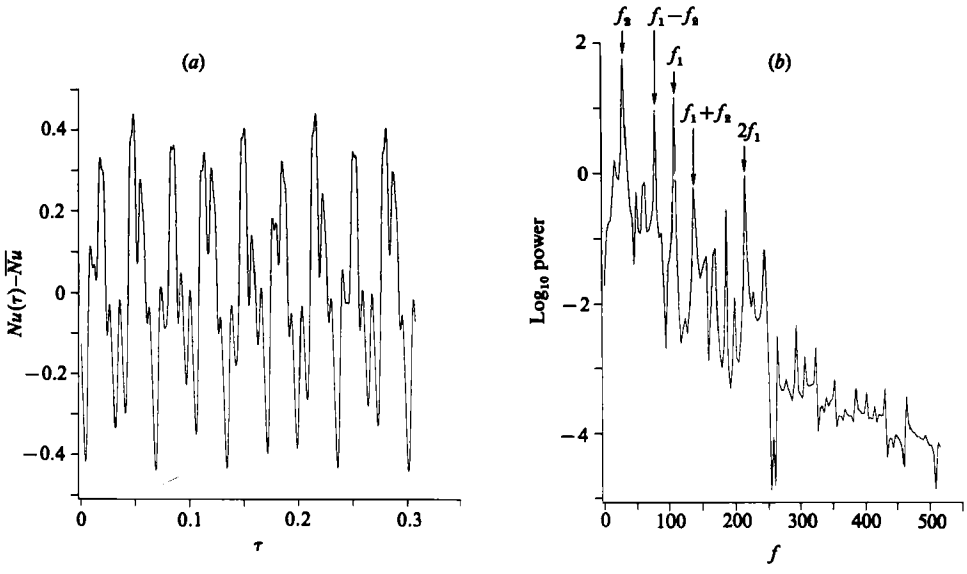

FIGURE 4. (*a*) The time series $Nu(\tau)-\overline{Nu}$ and (*b*) its power spectrum at $R = 540$ and $N = 26$.

$N = 26$ and 30. This is somewhat higher than the estimate $R_4 = 520$ based upon $N = 18$ (Schubert & Straus 1982). The characteristic frequency in this second simply periodic regime is independent of truncation number and is consistent with the functional relation $f \propto R^{\frac{3}{2}}$ (figure 2). Isotherms and streamlines for this case ($R = 650$) are shown in figure 7 at equally spaced times during a single oscillation. The flow and isotherm patterns in the core are essentially unchanged during an oscillation, in contrast to the variability of the core flow in the first simply periodic regime (figure 3). The tongue-like thermal blobs in the top and bottom boundary layers are prominent in figure 7. They grow slowly as the circulation carries them towards the corners where they are released into the rising or falling currents along the vertical walls. Each boundary layer contains a single thermal disturbance.

The variance in Nu, which falls with increasing R at the onset of the second P-regime, soon recovers (with a further increase in R) the level it had in QP_2 and stays at that magnitude (figure 6). The second P-regime exists for R up to 850. With a further increase in R it is replaced by a new type of time-dependent regime totally different from its predecessors.

Transition 5: $\mathrm{P}^{(2)} \rightarrow \mathrm{NP}$

The determination of R associated with the fifth transition from $\mathrm{P}^{(2)}$ to NP requires large truncation numbers. Because of insufficient resolution both $N = 20$ and $N = 26$ exhibit a spurious transition to multiple-frequency solutions at $R = 850$. However, the transition at $R = 850$ disappears when the truncation number is increased to $N = 30$. Our best estimate for R_5 based on $N = 30$, 36, 42 and 56 is somewhere between 850 and 1000.

Power spectra of $Nu(\tau)$ for R just above R_5 typically contain broadband background noise. The noise is a feature common to all the solutions we have obtained at $R > R_5$, independent of truncation number. Thus, because of the ubiquitous broadband noise, we follow Gollub & Bensen (1980) and refer to these solutions as non-periodic states (NP) even though they also have relatively sharp spectral peaks.

R	N	f_i or $\sum_i f_i$	f	Δf	$\log_{10}$ power
520	26	f_2	29		1.38
		f_1-f_2	75	± 3	0.32
		f_1	104		1.20
		f_1+f_2	134		−0.37
530*	26	f_1-f_2	65		−0.25
		f_2	81		−0.17
		f_1	147	± 3.2	0.48
		$2f_1-f_2$	208		−1.57
		f_1+f_2	224		−2.21
540	26	f_2	29		1.75
		f_1-f_2	78	± 3	0.93
		f_1	108		1.16
		f_1+f_2	137		−0.31
540	30	f_2	30		1.77
		f_1-f_2	75	± 5	0.65
		f_1	110		0.70
560	26	f_2	33		1.93
		f_1-f_2	78	± 3	1.22
		f_1	111		1.09
		f_1+f_2	143		−0.10
1000	36	f_3	12		0.68
		f_2-f_3	178		0.90
		f_2	190		2.11
		f_2+f_3	206		1.19
		$f_1-f_2-f_3$	250	± 3	1.30
		f_1-f_2	265		1.40
		$f_1-f_2+f_3$	278		0.64
		f_1-f_3	443		0.74
		f_1	456		1.59
		f_1+f_3	468		1.07
1000	42	f_3	14		1.28
		f_2-f_3	179		1.18
		f_2	193		2.41
		f_2+f_3	207		1.35
		f_2+2f_3	218		1.03
		$f_1-f_2-f_3$	249	± 2.8	1.46
		f_1-f_2	264		1.91
		$f_1-f_2+f_3$	278		0.91
		f_1-f_3	442		1.35
		f_1	456		1.87
		f_1-f_3	470		1.24
1000†	42	f_3	34		2.23
		f_2-f_3	115		1.75
		f_2	149		2.42
		f_2+f_3	183		1.78
		$f_1-f_2-f_3$	263		1.71
		f_1-f_2	297	± 4	1.59
		$f_1-f_2+f_3$	301		1.40
		f_1-f_3	412		0.84
		f_1	450		1.14
		f_1+f_3	485		1.42

TABLE 1. Powers and frequencies of spectral peaks in multiple-frequency regimes

* Initial conditions correspond to a $P^{(2)}$ state at higher R.

† The initial conditions are different.

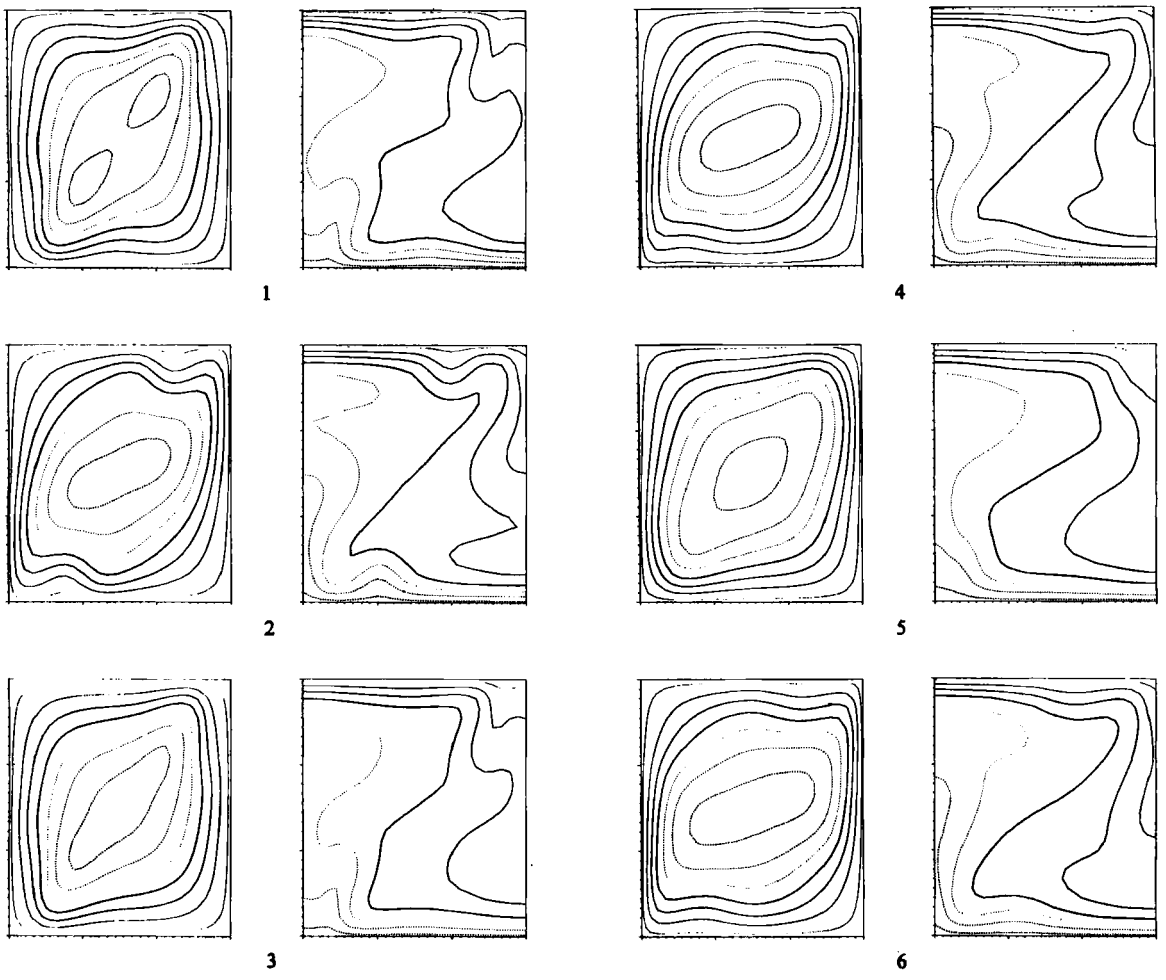

FIGURE 5. Streamline and isotherm patterns at equal intervals of time when $R = 540$ ($N = 26$). The non-dimensional time interval between successive figures is 0.0045 and the total elapsed time is 0.027 ($\tau_1 \equiv 1/f_1 = 0.0093, \tau_2 \equiv 1/f_2 = 0.033$). The isotherm and streamline contour intervals are the same as in figure 3.

Figure 8 shows (*a*) $Nu(\tau)$ and its (*b*) power spectrum for the NP state at $R = 1000$ ($N = 42$). The frequencies of the spectral peaks at $R = 1000$ are related to the frequencies of spectral peaks in the other time-dependent regimes. The primary frequency $f_1 = 456$ (table 1) is consistent with an extension of the $f \propto R^{\frac{1}{2}}$ trend of the second P-regime. The peak at the second frequency $f_2 = 193$ has the highest power, and the value of f_2 is near the extension of the $f \propto R^{\frac{1}{3}}$ trend from the first P-regime. The spectrum at $R = 1000$ contains power at a third independent frequency which we have identified as $f_3 = 14$. The frequencies, f_2 and the f_3 are sensitive to initial conditions. For example, by starting from a slightly different set of spectral coefficients, we obtained $f_2 = 156$ and $f_3 = 34$ at $R = 1000$. Nonetheless, both solutions are characterized by the presence of two incommensurate subfrequencies, and they are therefore fundamentally similar. The frequencies of the spectral peaks for both $R = 1000$ solutions are shown in figure 2.

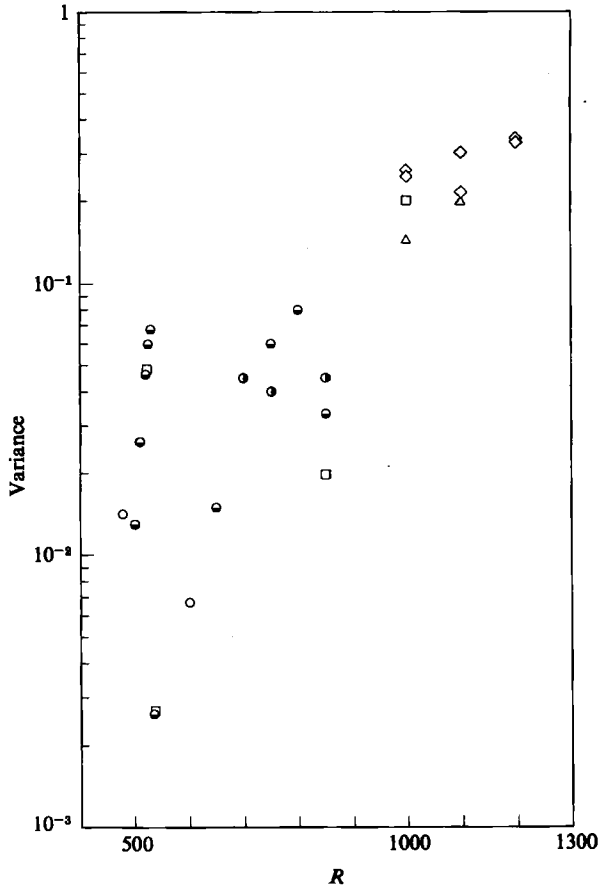

FIGURE 6. Variance of $Nu(\tau)$ time series as a function of Rayleigh number. Symbols are defined in figure 2.

In order to be certain that the NP state observed at $R = 1000$ is not a result of over-truncation, we carried out calculations with the truncation number increased to 56. The computations were continued until it was clear that the fundamental frequencies were well defined ($\tau \sim 0.75$). The power spectrum of the solution, although not dominated by the same frequencies as found in the $N = 42$ calculations, was found to be characterized by three independent frequencies and broadband background noise. (Again, the fact that the frequencies were not the same as found at $N = 42$ is probably a result of the dependence of the details of the solution on initial conditions.) This result confirms that convection at $R = 1000$ is, in fact, non-periodic (NP).

Flow patterns and isotherms at several times are shown in figure 9 for the $R = 1000$ solution presented in figure 8. The centre-symmetry characteristic of the S, $P^{(1)}$, QP_2 and $P^{(2)}$ regimes no longer exists. This is due to the growth of coefficients Φ_{jn} with $j+n =$ a positive odd integer. The growth of the 'odd' coefficients is very slow; integration for at least a half of the characteristic diffusion time ($\tau = 0.5$) is required for these coefficients to reach their full amplitude. Since initially assigned large values of the 'odd' coefficients decay monotonically with time at $R = 850$, the growth of these coefficients at $R = 1000$ should be considered a special characteristic of the NP-regime. Figure 9 shows that there are at least two thermal blobs in each of the

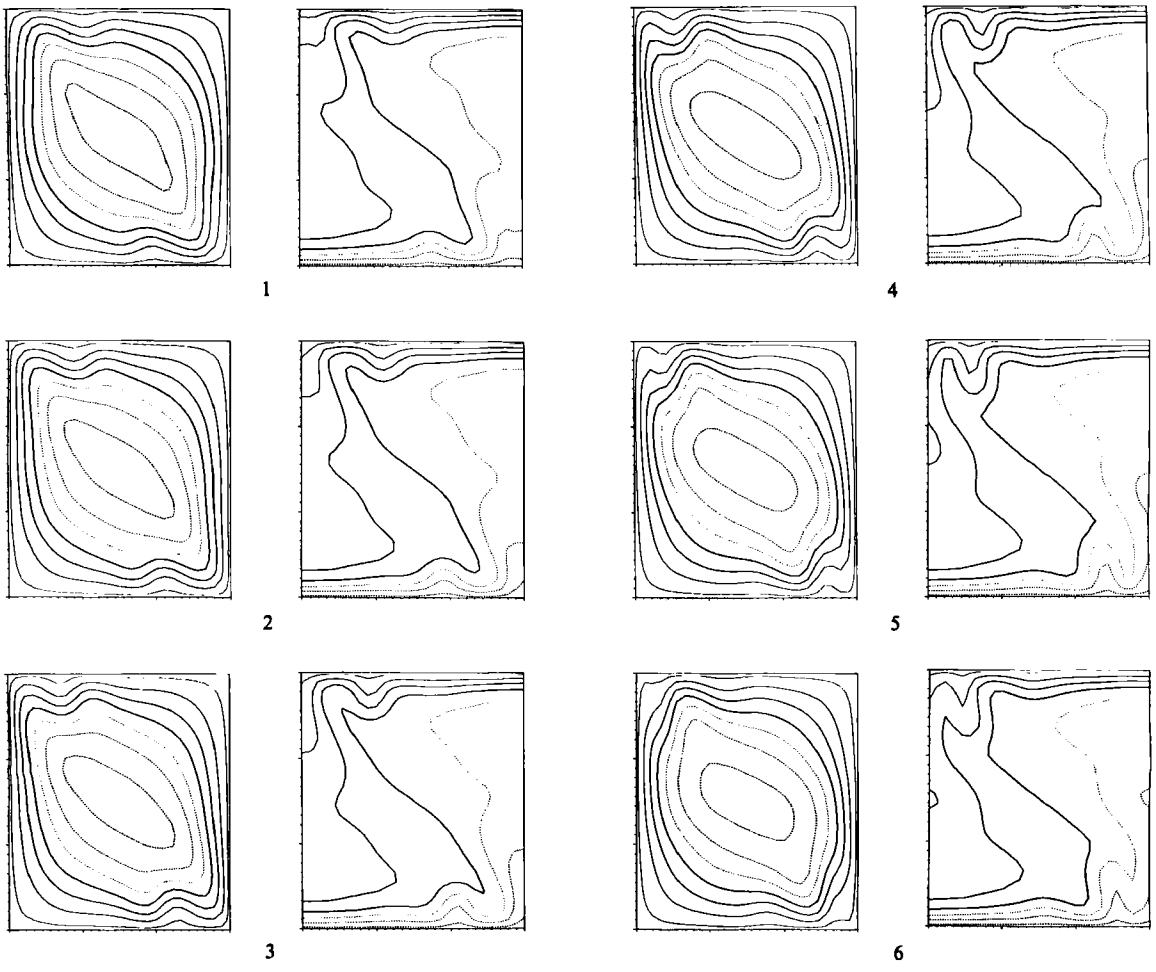

FIGURE 7. Streamline and isotherm patterns at equal intervals of time during a single oscillation when $R = 650$ ($N = 18$). The non-dimensional time interval between successive figures is 0.00056 and the total elapsed time is 0.0044 ($\tau_1 \equiv 1/f_1 = 0.0050$). The isotherm contour interval is 0.15 and the stream-function contour interval is 3.3.

boundary layers. These thermals are thus generated at a much faster rate in the NP-regime than they are at lower R. The flow in the core region is rather similar to that in the second periodic regime; there is no strong variability in the pattern from one instant of time to another. The disturbances are largely confined to the boundary layers. The variance in $Nu(\tau)$ increases by an order of magnitude in the transition from $P^{(2)}$ to NP (figure 6).

Transition 6: NP → *time-dependent multiple cells?*

For $N = 30$ or 36 and $R = 1200$ single-cell time-dependent convection no longer exists. The flow splits up into four or five vortices, evidently as a result of penetration by the thermal plumes into the core (figure 10). The sizes of the vortices and their senses of rotation vary throughout the flow field. The flow patterns of these time-dependent multiple-cell solutions are, therefore, fundamentally different from the steady multiple cells of linear theory. The time-averaged Nusselt number

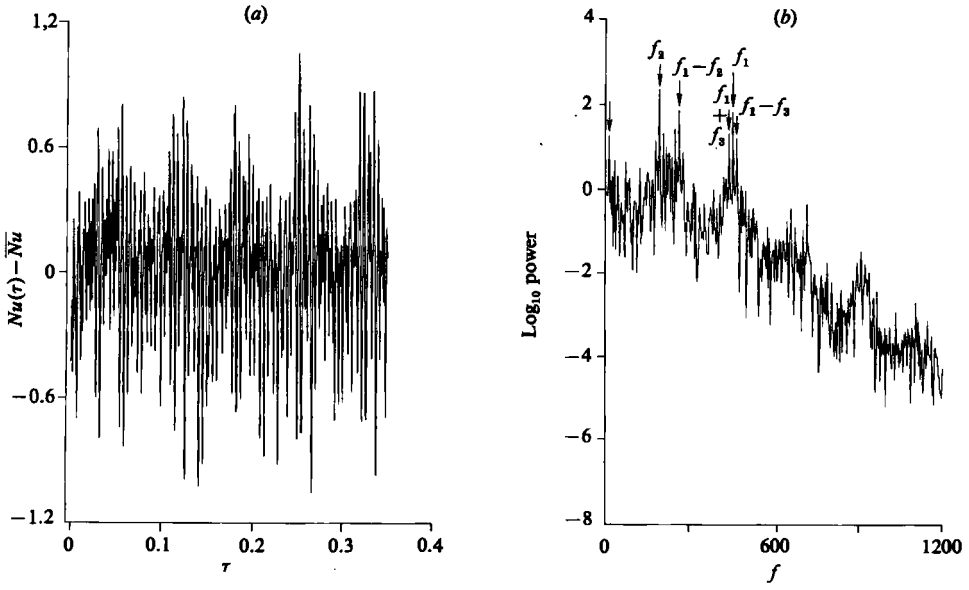

FIGURE 8. (*a*) The time series $Nu(\tau)-\overline{Nu}$ and (*b*) its power spectrum at $R = 1000$ and $N = 42$. There is a broadband noise component of the spectrum in addition to some sharp spectral peaks.

decreases by approximately 20% from the value it would have had if single-cell convection had persisted, and the variance increases by an order of magnitude from its level for the NP states. The power spectrum contains no consistently identifiable peak; the power decays slowly and monotonically, in an average sense, as frequency increases (figure 11).

The transition to time-dependent multiple cells described above is, however, an artifact of over-truncation. With the higher truncation number of 42 the flow at $R = 1200$ is indeed single-cell NP convection, just as it is at the lower Rayleigh numbers of 1000 and 1100. However, we speculate that the spurious bifurcation to time-dependent multiple cells at $R = 1200$ and low N might indicate that a similar transition actually occurs at higher R.

4. Discussion

4.1. *Time-averaged Nusselt number*

It has been established in previous calculations (Schubert & Straus 1982) that $\overline{Nu} \propto R^{\frac{2}{3}}$ for convection in the first simply periodic regime $P^{(1)}$. The results reported here confirm this $\overline{Nu}$–R relation for R in $P^{(1)}$ (figure 12). In addition, they show that a different $\overline{Nu}$–R power-law relation applies in the second simply periodic regime $P^{(2)}$. For R in $P^{(2)}$, $\overline{Nu} \propto R^{\frac{11}{10}}$ is a good fit, in the least-squares sense, to the numerically determined values of the time-averaged Nusselt number (figure 12). The differences in the slopes of the $\overline{Nu}$–R power-law relations between the two simply periodic flow regimes can be understood in terms of the characteristic flow structures of the regimes. The formation of thermal blobs in the $P^{(1)}$ regime (figure 3) tends to thicken the boundary layers along their entire length. This tends to offset the thinning of the boundary layers that normally accompanies increases in R and consequently tends to reduce the rate at which the heat transport increases with R. In contrast, thermal

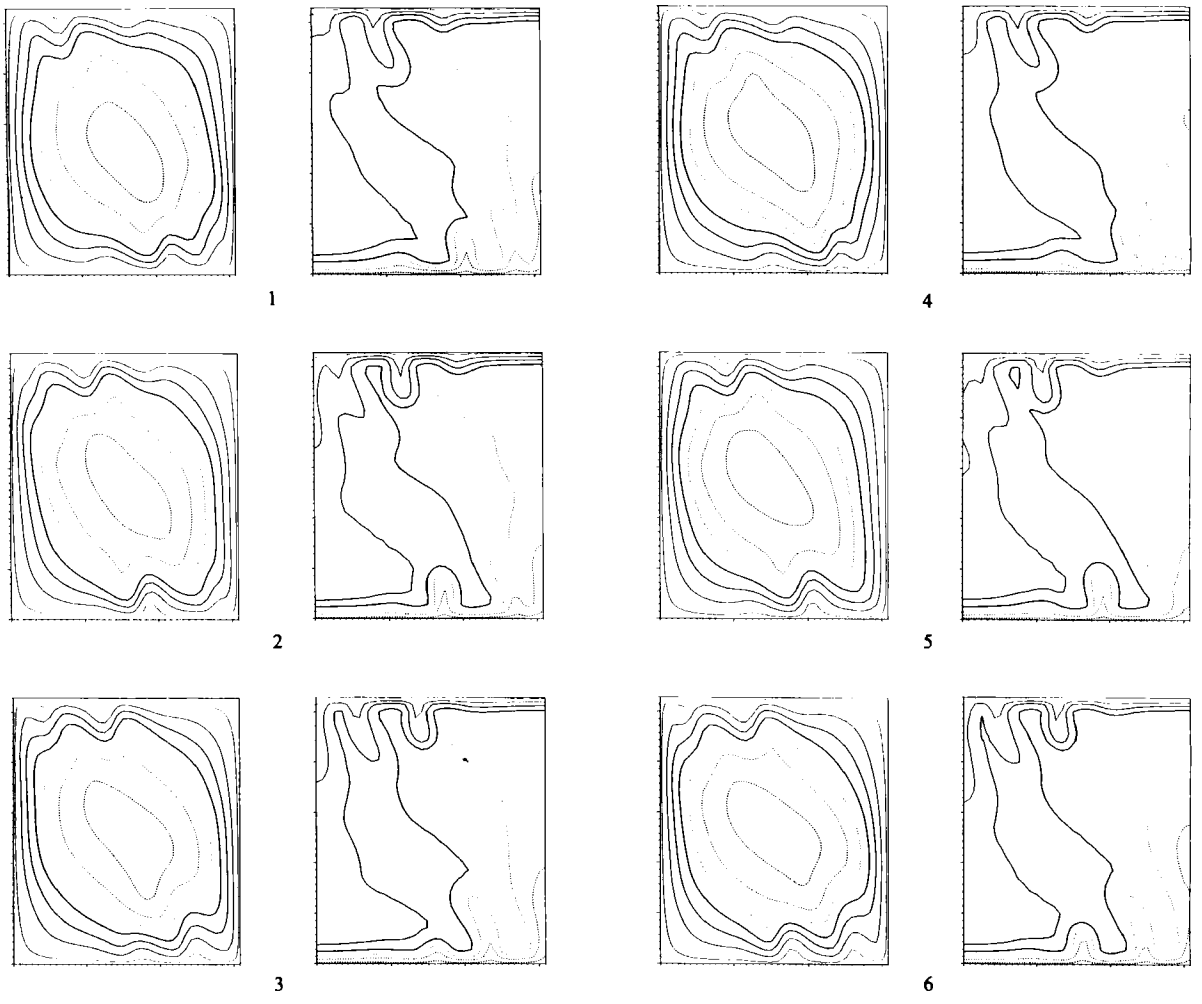

FIGURE 9. Streamline and isotherm patterns at equal time intervals for $R = 1000$ ($N = 42$). The non-dimensional time interval between successive figures is 0.0016 and the total elapsed time is 0.0094 ($\tau_1 \equiv 1/f_1 = 0.0022$, $\tau_2 \equiv 1/f_2 = 0.0053$, $\tau_3 \equiv 1/f_3 = 0.053$). The isotherm contour interval is 0.15 and the stream-function contour interval is 5.

blobs in the $P^{(2)}$ regime are more localized, and most of the horizontal walls are covered by undisturbed thermal boundary layers. Boundary-layer thinning with increasing R occurs with less opposition from the development of broad thermal plumes, and heat transfer can increase more rapidly with increases in R. The flow patterns of figure 7 also show that the discharged thermals do not significantly affect the core flow. Thus, convection in the $P^{(2)}$ regime can be properly characterized as a boundary-layer-type flow. The increase of the average Nusselt number with R approximately follows the $R^{\frac{11}{16}}$ trend into the NP regime (figure 12).

A simple scale analysis based on boundary-layer approximations can predict the slope of the $\log \overline{Nu}$–$\log R$ relation at the relatively high Rayleigh numbers of the $P^{(2)}$ regime. The analysis is similar to one presented by Kimura & Bejan (1984) for convection driven by constant heat flux from the side and it has been applied to the present problem by Bejan (1984). Advection of heat by the plumes is responsible for

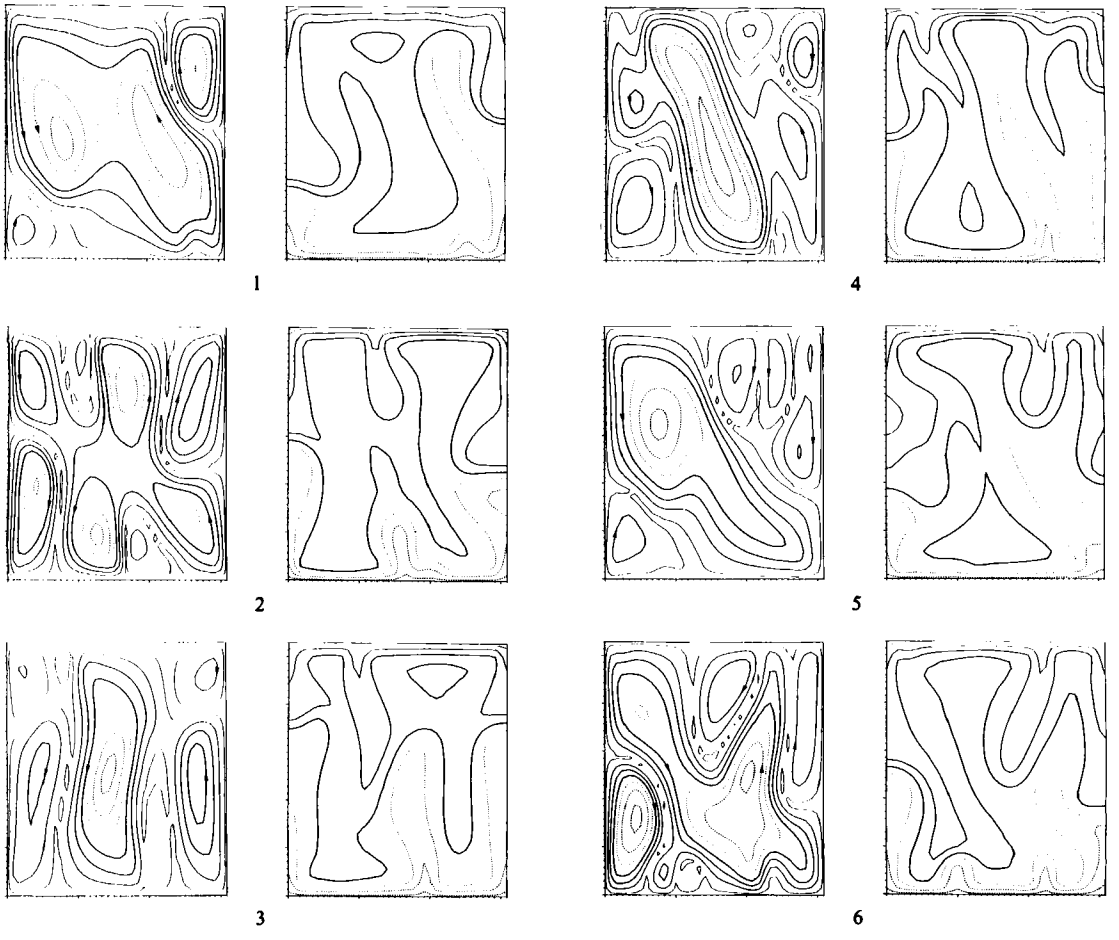

FIGURE 10. Streamline and isotherm patterns at equal time intervals for a non-periodic solution at $R = 1200$ ($N = 36$). The non-dimensional time interval between successive figures is 0.0035 and the total elapsed time is 0.021. The isotherm contour interval is 0.15 and the stream-function ϕ_ξ contour interval is 3.5.

heat transport across the core, while vertical conduction transfers heat across the boundary layers. By matching these heat transports, it is possible to deduce that

$$Nu \propto R. \tag{4.1}$$

This is very close to the result $Nu \propto R^{11}_{10}$ that we obtained by a least-squares fit of calculated heat transports in the Rayleigh-number range 550–1100. The agreement between (4.1) and $Nu \propto R^{11}_{10}$ further substantiates the classification of convection in P as a boundary-layer flow.

4.2. *Mechanism of oscillation*

One physical process that can lead to oscillatory convection is the gravitational instability of thermal boundary layers over heated or cooled horizontal surfaces (Howard 1964). When the Rayleigh number based on the local thickness of the boundary layer and the temperature difference across it exceeds the critical value, the layer becomes unstable and eventually breaks up by forming a buoyant hot spot

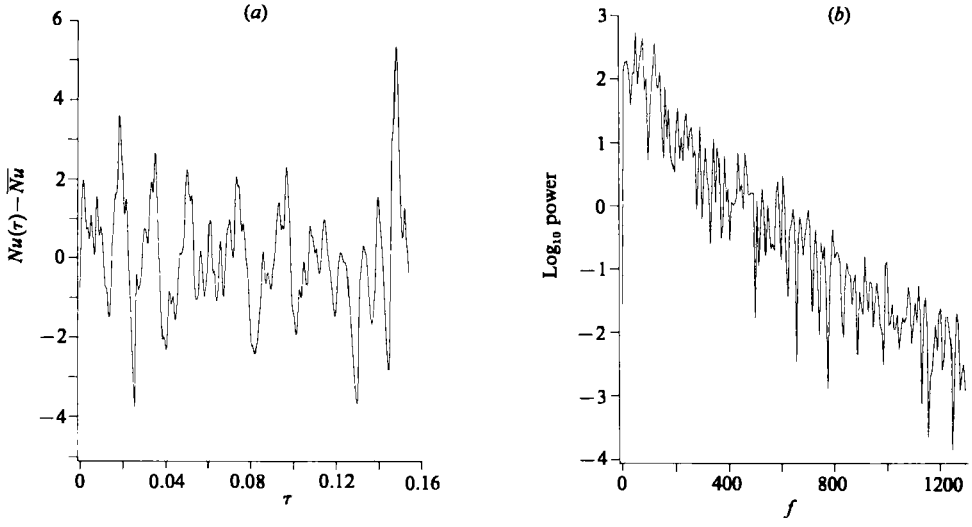

FIGURE 11. (*a*) The time series $Nu(\tau)-\overline{Nu}$ and (*b*) its power spectrum at $R = 1200$ and $N = 36$. There is no consistently identifiable peak in the power spectrum.

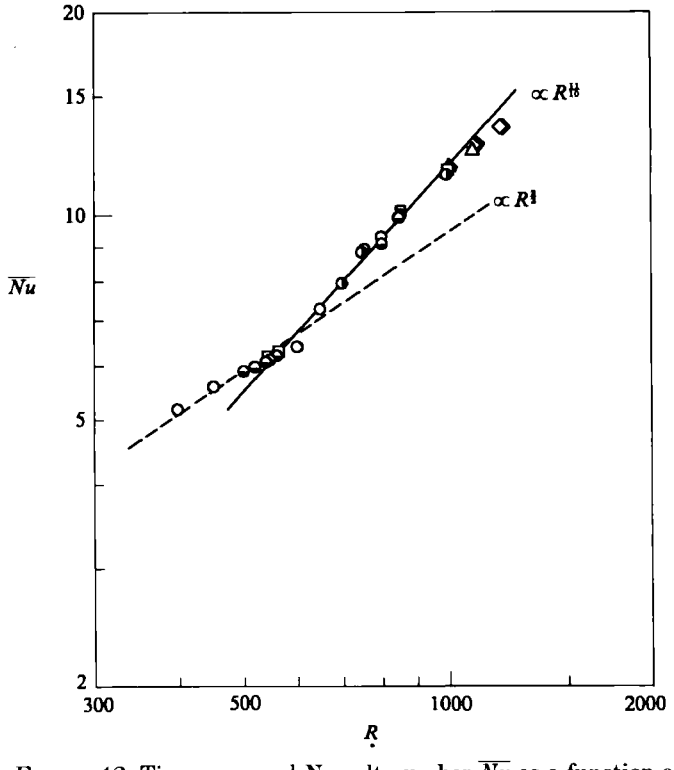

FIGURE 12. Time-averaged Nusselt number $\overline{Nu}$ as a function of R. Symbols are defined in figure 2.

or plume. The occurrence of boundary-layer instability has been confirmed experimentally by Sparrow, Husar & Goldstein (1970) with water as the working fluid.

Moore & Weiss (1973) encountered oscillatory behaviour in their numerical simulations of convection of an ordinary fluid. Their results (figure 3 in Moore & Weiss 1970) do not provide any evidence of buoyancy instability of the thermal boundary layers. Instead, they show that the tips of the vertical thermal plumes are periodically pinched off after the plumes turn the corners and become horizontal. The pinched-off thermal blobs are advected as isolated hot or cold spots past the horizontal thermal boundary layers and eventually dissipate by diffusion. When a hot (cold) thermal blob passes the cold (hot) thermal boundary layer at the top (bottom) of the convection cell it creates a disturbance of the layer. This mechanism for producing oscillatory behaviour depends on the interaction of isolated thermal blobs with the boundary layers. Welander (1967) and Keller (1966) invoked a similar interaction to explain the convective oscillations of fluid loops.

According to the temperature fields shown in figures 3, 5, 7 and 9, buoyancy instability of the horizontal thermal boundary layers appears to be the primary source of temporal variability in the examples of porous-medium thermal convection in this study (see Gary *et al.* 1982 for a similar observation). The time period taken to generate a thermal corresponds to one cycle of the Nusselt-number oscillation (see figures 3 and 7). The thermals discharged along the vertical boundaries dissipate by diffusion before they reach the opposite horizontal boundaries. Thus there is no thermal-blob–boundary-layer interaction of the type involved in the Moore & Weiss (1973) study.

Horne & O'Sullivan (1978) and Horne & Caltagirone (1980) have also investigated the sources of time dependence in porous-medium thermal convection. They found that, though the boundary-layer Rayleigh number is supercritical, the growth time of a thermal varies as $R^{-\frac{3}{2}}$, (this agrees with our finding in the $P^{(2)}$ regime) and not as R^{-2}, as might be expected if Howard's mechanism were the source of generation of thermals. However, Howard's model applies to the diffusive growth of a boundary layer in a stationary medium of infinite extent. In this case, the boundary-layer thickness δ varies as $t^{\frac{1}{2}}$ and since δ varies as R^{-1} the characteristic frequency of oscillations caused by buoyancy instability of the boundary layer is $\propto R^2$. However, things are more complicated in high-Rayleigh-number porous-medium convection. The horizontal boundary layer thickens with distance from the corner, but not in a simple way because of the influx of material from the interior of the cell into the boundary layer. In addition, the horizontal velocity in the boundary layer varies with distance from the corner. These complications preclude a simple rationale for the $f \propto R^{\frac{3}{2}}$ scaling in the $P^{(2)}$ regime. The isotherm and streamline patterns nevertheless confirm that buoyancy instability of the horizontal thermal boundary layers is the source of the oscillatory behaviour of the high-Rayleigh-number $P^{(2)}$ solutions.

4.3. *Similarities to Hele–Shaw convection*

There are interesting similarities between time-dependent convection in a porous medium and in a Hele–Shaw cell because inertia effects are negligible in both flows. Time-dependent Hele–Shaw convection has been found to exhibit hysteresis (Koster & Müller 1984), i.e. the state at a given Rayleigh number can depend on whether it is attained by increasing or by decreasing the Rayleigh number. We have found analogous behaviour for states in the multiple-frequency QP_2 regime ($R = 530$, table 1). A comparison of the frequencies given for $R = 520$, 530 and 540 in table 1 indicates that the system tends to retain the dominant frequency inherited from its predecessor

states. It is possible that the bifurcation Rayleigh numbers separating the QP_2 interval from its adjacent simply periodic regimes depend on whether the transitions are crossed in the directions of increasing or decreasing R.

Reverse transitions, i.e. bifurcations from more to less disorder with increasing R, occur in both porous medium and Hele–Shaw convection (Koster & Müller 1984). Porous-medium convection exhibits the $QP_2 \rightarrow P$ transition (Schubert & Straus 1982). In the Hele–Shaw experiment (Koster & Müller 1984) double-cell oscillatory convection also undergoes a $QP \rightarrow P$ transition. With increasing R this type of convection eventually evolves into 4-cell steady convection. We speculate that single-cell, time-dependent convection in a porous layer could eventually evolve (with increasing R) into a multiple-cell, time-dependent or steady-state circulation.

4.4. *Route to chaotic convection*

A system of nonlinear ordinary differential equations can evolve (with monotonic change in a dimensionless parameter that governs the solution) to a state of chaos by at least two routes. One path involves the introduction of a third incommensurate frequency into the time-variable state (Ruelle & Takens 1971). The other consists of a sequence of period-doubling bifurcations (Feigenbaum 1978). The numerical experiments of this paper evolve to chaos with increasing R according to the scheme of Ruelle & Takens (1971). The introduction of the third incommensurate frequency leads the system to an increasingly complex state that can be seen as high background noise in the power spectrum of figure 8.

Over-truncated systems with $N = 20$ and 26 evolve toward chaos along different paths. With $N = 20$, the onset of the second multiple-frequency regime takes place at $R = 850$ by the introduction of two subfrequencies whose ratios to the primary frequency are $f_3/f_2/f_1 = 1/2/4$, i.e. period doubling occurs. Gollub & Benson (1980) have demonstrated the occurrence of period doubling in the thermal convection of ordinary fluids for certain values of the Prandtl number and cell aspect ratio. With $N = 26$, the onset of the second multiple-frequency regime also takes place at $R = 850$, but it occurs via the introduction of two incommensurate frequencies, analogous to the transitions that take place at $R = 1000$ for the higher truncation levels. The $N = 26$ single-cell solutions become time-dependent multiple-cell solutions at $R = 1000$.

Symmetry breakdown associated with the growth of odd coefficients Φ_{nj} ($n+j$ = odd integer) is a characteristic common to all the NP-states independent of truncation level. The growth of these coefficients is not a numerical artifact or instability. Odd coefficients established through calculations with $N = 20$ and 26 decay when the truncation number is raised to $N = 30$, and the system restores its symmetry. However, we have never observed any decay of odd coefficients in the NP regime at truncation levels of $N = 36$, 42 and 56. McLaughlin & Orszag (1982) have also noted a link between symmetry breaking and the onset of chaos in the numerical simulation of Rayleigh–Bénard convection in air.

5. Concluding remarks

The major new findings we report are: (i) the route to chaos in porous-medium thermal convection is $S \rightarrow P^{(1)} \rightarrow QP_2 \rightarrow P^{(2)} \rightarrow NP$, which involves the introduction of two incommensurate frequencies into a simply periodic state according to the theory of Ruelle & Takens (1971), and (ii) the existence of hysteresis in a multiple-frequency QP_2 regime. Overtruncation has serious consequences in studies of time-dependent

convection and must be zealously guarded against lest physical reality be attributed to spurious bifurcations and transition sequences (Marcus 1981). For example, we have seen that over-truncation can lead to chaotic convection through the process of period doubling. Overtruncation generally leads to overly complex behaviour in time-dependent solutions, a point that has also been emphasized by Curry *et al.* (1984) in their recent study of the route to chaos in Rayleigh–Bénard convection of an ordinary viscous fluid with free-slip boundaries. It should be remembered that steady multiple-cell solutions also exist at the high Rayleigh numbers, where we have found periodic, quasi-periodic and chaotic single-cell convection. It would be of interest to see if Steen's (1984) phase-space approach could be generalized to determine the probability of realizing the different modes of high-Rayleigh-number convection. Finally, it would be of value to determine how the route to chaos might be affected by different cell aspect ratios and the additional degree of freedom provided by the third dimension. Such studies are now in progress.

This research received support from the National Science Foundation (Grant MEA 82-18600), the University of California, and the Aerospace Sponsored Research Program. We thank H. E. Cogen for help in carrying out a number of the numerical calculations.

REFERENCES

BEJAN, A. 1984 *Convective Heat Transfer*, p. 412. Wiley.

CALTAGIRONE, J. P. 1974 Convection naturelle fluctuante en milieu poreux. *C.R. Acad. Sci. Paris* **278 B**, 259.

CURRY, J. H., HERRING, J. R., LONCARIC, J. & ORSZAG, S. A. 1984 Order and disorder in two- and three-dimensional Bénard convection. *J. Fluid Mech.* **147**, 1.

FEIGENBAUM, M. J. 1978 Quantitative universality for a class of nonlinear transformations. *J. Stat. Phys.* **19**, 25.

GARY, J., KASSOY, D. R., TADJERAN, H. & ZEBIB, A. 1982 The effects of significant viscosity variation on convective heat transport in water-saturated porous media. *J. Fluid Mech.* **117**, 233.

GOLLUB, J. P. & BENSON, S. V. 1980 Many routes to turbulent convection. *J. Fluid Mech.* **100**, 449.

GOTTLIEB, D. & ORSZAG, S. A. 1977 *Numerical Analysis of Spectral Methods: Theory and Applications*. SIAM.

HORNE, R. N. & CALTAGIRONE, J. P. 1980 On the evolution of thermal disturbances during natural convection in a porous medium. *J. Fluid Mech.* **100**, 385.

HORNE, R. N. & O'SULLIVAN, M. J. 1978 Origin of oscillatory convection in a porous medium heated from below. *Phys. Fluids* **21**, 1260.

HOWARD, L. N. 1964 Convection at high Rayleigh number. In *Proc. 11th Intl Cong. Appl. Mech., Munich*, p. 1109. Springer.

KELLER, J. B. 1966 Periodic oscillations in a model of thermal convection. *J. Fluid Mech.* **26**, 599.

KIMURA, S. & BEJAN, A. 1984 The boundary layer natural convection regime in a rectangular cavity with uniform heat flux from the side. *Trans. ASME* C: *J. Heat Transfer* **106**, 98.

KOSTER, J. N. & MÜLLER, V. 1984 Oscillatory convection in vertical slots. *J. Fluid Mech.* **139**, 363.

LAPWOOD, E. R. 1948 Convection of a fluid in a porous medium. *Proc. Camb. Phil. Soc.* **44**, 508.

MCLAUGHLIN, J. B. & ORSZAG, S. A. 1982 Transition from periodic to chaotic thermal convection. *J. Fluid Mech.* **122**, 123.

MARCUS, P. S. 1981 Effects of truncation in modal representations of thermal convection. *J. Fluid Mech.* **103**, 241.

MOORE, D. R. & WEISS, N. O. 1973 Two-dimensional Rayleigh–Bénard convection. *J. Fluid Mech.* **58**, 289.

ORSZAG, S. A. 1971 Numerical simulation of incompressible flows within simple boundaries. *Stud. Appl. Math.* **50**, 293.

RUELLE, D. & TAKENS, F. 1971 On the nature of turbulence. *Commun. Math. Phys.* **20**, 167.

SCHUBERT, G. & STRAUS, J. M. 1979 Three-dimensional and multicellular steady and unsteady convection in fluid-saturated porous media at high Rayleigh numbers. *J. Fluid Mech.* **94**, 25.

SCHUBERT, G. & STRAUS, J. M. 1982 Transitions in time-dependent thermal convection in fluid-saturated porous media. *J. Fluid Mech.* **121**, 301.

SPARROW, E. M., HUSAR, R. B. & GOLDSTEIN, R. J. 1970 Observations and other characteristics of thermals. *J. Fluid Mech.* **41**, 793.

STEEN, P. H. 1984 Pattern selection for finite-amplitude convection states in boxes of porous media. *J. Fluid Mech.* **136**, 219.

STRAUS, J. M. 1974 Large amplitude convection in porous media. *J. Fluid Mech.* **64**, 51.

STRAUS, J. M. & SCHUBERT, G. 1979 Three-dimensional convection in a cubic box of fluid-saturated porous material. *J. Fluid Mech.* **91**, 155.

STRAUS, J. M. & SCHUBERT, G. 1981 Modes of finite-amplitude three-dimensional convection in a cubic box of fluid-saturated porous material. *J. Fluid Mech.* **103**, 23.

WELANDER, P. 1967 On the oscillatory instability of a differentially heated fluid loop. *J. Fluid Mech.* **29**, 17.